The effects of intraparticle structure and interparticle interactions on the magnetic hysteresis loop of magnetic nanoparticles

Zoe Boekelheide,[1,2,a)] Jackson T. Miller,[1] Cordula Grüttner,[3] and Cindi L. Dennis[2,b)]

AFFILIATIONS

[1]Department of Physics, Lafayette College, Easton, Pennsylvania 18042, USA
[2]Material Measurement Laboratory, NIST, Gaithersburg, Maryland 20899, USA
[3]Micromod Partikeltechnologie GmbH, Friedrich-Barnewitz-Str. 4, D-18119 Rostock, Germany

[a)]boekelhz@lafayette.edu
[b)]cindi.dennis@nist.gov

ABSTRACT

Technologically relevant magnetic nanoparticles for biomedicine are rarely noninteracting single-domain nanoparticles; instead, they are often interacting, with complex physical and magnetic structures. In this paper, we present both experimental and simulated magnetic hysteresis loops of a system of magnetic nanoparticles with significant interparticle interactions and a well-defined intraparticle structure which are used for magnetic nanoparticle hyperthermia cancer treatment. Experimental measurements were made at 11 K on suspensions of magnetic nanoparticles dispersed in H_2O which have been frozen in a range of applied magnetic fields to tune the interparticle interactions. Micromagnetic simulations of hysteresis loops investigated the roles of particle orientation with respect to the field and of particle chaining in the shape of the hysteresis loops. In addition, we present an analysis of the magnetic anisotropy arising from the combination of magnetocrystalline and shape anisotropy, given the well-defined internal structure of the nanoparticles. We find that the shape of the experimental hysteresis loops can be explained by the internal magnetic structure, modified by the effects of interparticle interactions from chaining.

https://doi.org/10.1063/1.5094180

I. INTRODUCTION

Magnetic nanoparticles (MNPs) have been the focus of significant research due to the large number of potential applications in biomedicine and industrial fields. These include biomedical applications such as hyperthermia,[1,2] drug delivery,[3] and imaging.[4,5] They are also used as ferrofluids for shock absorption[6,7] and other industrial purposes. While there has been significant progress in developing MNPs for specific applications and understanding simple models of MNPs, the impact of intraparticle structure of MNPs and interparticle interactions in ensembles of MNPs on the measured magnetic behavior needs further study.

It is well-established that the magnetic hysteresis loop, or the $M(H)$ curve, for MNPs is generally significantly different from that of the bulk material. Bulk magnets typically form magnetic domains and, when the applied field is cycled, the magnetization reverses via domain wall motion or domain nucleation and growth. Particles smaller than about 100 nm (depending upon the magnetic properties, generally approximated by the bulk material properties) are assumed to be single domain[8,9] and to reverse via coherent rotation.[10]

The well-known Stoner-Wohlfarth model[10] is used when the MNP is single domain and the atomic magnetic moments can be treated as one large moment (the "macrospin" approximation). Typically, the MNP is also assumed to have uniaxial magnetic anisotropy. Then, the total energy (Zeeman and anisotropy energy) of the MNP is considered and the direction for the magnetic moment $\vec{m}$ is found which satisfies a local energy minimum. The characteristic hysteresis behavior occurs due to the persistence of the magnetization in a (metastable) local energy minimum until the energy barrier for switching becomes small. The Stoner-Wohlfarth model is often a reasonable approximation for small, single-domain

MNPs, though it typically overestimates the coercivity.[11] Many researchers have used Stoner-Wohlfarth models to represent MNPs around 10 nm in size. The simplest case is the noninteracting, single-domain model, but this model can be extended to include dynamics and the effects of temperature;[12] interparticle interactions between single-domain MNPs have been considered in other models.[13–15]

However, properties of MNPs such as structure and shape can disrupt the balance of energies resulting in noncollinear spins. It has previously been experimentally established that the assumption of "single domain" for MNPs does not generally hold.[16] The exact spin structure is highly dependent upon the synthesis conditions, structure of the MNP, and any crystals within it.

To model $M(H)$ in the case where atomic magnetic moments within the MNP are not collinear and the Stoner-Wohlfarth model is invalid, micromagnetic models are required. In a micromagnetic model, the MNP is discretized into cells with sizes typically on the order of nanometers. The atomic magnetic moments are then assumed to be collinear within each cell. The next step is to either minimize the total energy (Zeeman, anisotropy, demagnetization, and exchange energy) or solve the Landau-Lifshitz or Landau-Lifshitz-Gilbert equation[17,18] to find the direction of $\vec{m}$ for each cell. One of the downsides to micromagnetic simulations is that they do not naturally include temperature. There has been recent work to expand micromagnetic simulations to include thermal effects,[19] but issues remain. Computational finite-difference implementations of micromagnetic models include OOMMF (Object Oriented Micromagnetic Framework)[20] and MuMax,[19] among others.

Finally, for phenomena occurring at the atomic level, atomistic models may be used.[16,21,22] Atomistic models have typically been used on systems of individual, noninteracting MNPs no larger than ~10 nm due to issues of computational power. Real MNPs, including the MNPs discussed here, are often larger than this and can form complex systems with both interparticle and intraparticle magnetic interactions and structure playing an important role in the magnetic behavior.

In this paper, we present experimental work and accompanying simulations on a complex MNP system. This system is highly relevant for applications, showing success in animal models of magnetic nanoparticle hyperthermia cancer treatment.[23,24] The MNPs, with an ~50 nm diameter core, are significantly larger than the ~10 nm size that has been the basis of most theoretical studies. The MNPs described here have both significant intraparticle structure in the form of parallelepiped-shaped crystallites and magnetic domains, and significant interparticle interactions, which are thought to enhance their heating ability for hyperthermia applications.

In magnetic nanoparticle hyperthermia cancer treatment, the heat released by the MNPs under an alternating magnetic field is proportional to the area enclosed by the magnetic hysteresis loop. Thus, understanding the factors determining the magnetic hysteresis loop is paramount to optimizing this cancer treatment. In both experimental and theoretical studies, reports of the heat generated by MNPs under an alternating magnetic field vary by orders of magnitude depending on the details of the MNPs used and the study conditions. The role of both interparticle and intraparticle interactions in explaining these disparities has been debated and is still unclear.[2,13–15,25] Most experimental measurements of heat output under hyperthermia conditions (measured by the specific loss power or SLP and also called the specific absorption rate or SAR) are measured on MNPs colloidally suspended in fluid rather than MNPs *in vivo*. Understanding how interparticle interactions between MNPs which are free to move and form structures such as chains is important to understanding the results of such measurements and how they relate to clinical conditions.

This paper presents DC hysteresis loop measurements on MNPs in frozen suspensions, dispersed in H_2O, at cryogenic temperatures (11 K), as a function of applied magnetic field while cooling. The choice of magnetic field applied during cooling influences the balance of energies present in the suspension, most especially the interparticle interactions from chaining, allowing us to study the influence of these interactions on the magnetic behavior. Freezing the suspension prevents motion of the MNPs, and the cryogenic temperature decreases the thermal fluctuations of the magnetic moments. The $M(H)$ loops obtained under these experimental conditions have many similarities with those which would occur under magnetic nanoparticle hyperthermia treatment conditions. In both cases (DC hysteresis loop at cryogenic temperatures vs dynamic hysteresis loop at ~100 kHz frequencies and physiological temperatures), the average time for thermal fluctuation-driven magnetization switching is quite long compared to the field cycle time ($\omega\tau \gg 1$). In addition, the average time for physical rotation of these MNPs in fluid suspension is long (~1 ms) compared to the field cycle time under hyperthermia conditions, so the comparison to a frozen sample is relevant.

We compare these experimental results to a micromagnetic model of MNPs with an internal magnetic structure and interparticle interactions similar to that exhibited by the experimental system. An added benefit to working at cryogenic temperatures is that the micromagnetic modeling is most accurate at $T = 0$ K. The combination of experiments and simulations helps us to better understand the role/impact of both the internal magnetic structure and the interparticle interactions on the magnetic hysteresis loops.

II. METHODS

A. Physical characterization of nanoparticles

The MNPs studied here are the bionized nanoferrite (BNF) nanoparticles synthesized via a high temperature/high pressure homogenization process.[26] Extensive physical and magnetic characterization has been previously performed on the BNFs,[24,26–32] due to their technological relevance, and is summarized here. The BNFs are composed of a solid iron oxide core, which is predominantly magnetite (though multiple compositions are present), and coated twice with a dextran shell which was then cross-linked with an amine ($-NH_2$) functionalization. The core is approximately 50 nm in diameter with a polydispersity of 30%. The dextran shell is approximately 40 nm thick based on hydrodynamic size. The BNFs are dispersed in H_2O with a concentration of 25.1 ± 0.2 mg/ml (where the error represents 1σ).

The solid core is composed of multiple crystallites, each of which is shaped like a parallelepiped. Magnetically, the MNPs are multidomain. The magnetic domains are also parallelepiped-shaped, though they are not necessarily coincident with the crystallites.[27] Average dimensions ($\pm 1\sigma$) for the parallelepiped-shaped crystallites are $(66 \pm 10\,\text{nm}) \times (26 \pm 2\,\text{nm}) \times (8 \pm 1\,\text{nm})$.[28] This internal

structure is shown schematically in Fig. 1. Experimental evidence does not indicate any preferred crystallographic orientation for the core.[28] Therefore, there is no preferred orientation for the magnetocrystalline easy axes of the crystallites. In addition, strong magnetic dipolar interactions between MNPs are seen and linear chains of MNPs form in the direction of an applied magnetic field.[29,30]

B. Field-cooled magnetic characterization of nanoparticles

Field-cooled magnetic characterization was performed on a Superconducting QUantum Interference Device Vibrating Sample Magnetometer (SQUID VSM) by Quantum Design.[33] A LakeShore liquid capsule[33] was filled with 28.3 mg of the liquid sample and sealed with epoxy. Measurements were performed on the frozen sample at 11 K after cooling from room temperature (300 K) in a fixed magnetic field H_{cool} between 0 mT and 7 T (specifically, 0 mT, 7 mT, 20 mT, 40 mT, 70 mT, 2 T, and 7 T). The magnetic field gradient in this system is negligible. The DC hysteresis loop $M(H)$ was measured from +7 T to −7 T and back to +7 T five times. Here, "DC" refers to field cycle times of more than an hour. Multiple field cycles were utilized to remove small asymmetry effects in H (less than 7 mT), which may arise from uncompensated surface spins on the MNPs[34,35] or artifacts from remanent magnetic fields in the superconducting magnet of the SQUID VSM.[36–38]

To further investigate the origins of the hysteresis loop shape dependence on cooling field, we performed additional experiments using a two-step field cooling procedure. In these experiments, the sample was initially cooled from 300 K to 180 K (through the freezing point of H_2O including any additional suppression from the dextran) in a fixed magnetic field (either 7 T or 0 mT) and then cooled from 180 K to 11 K in a different field (20 mT). Again, the field was cycled five times and the data from the fifth field cycle were used to remove slight asymmetry in H.

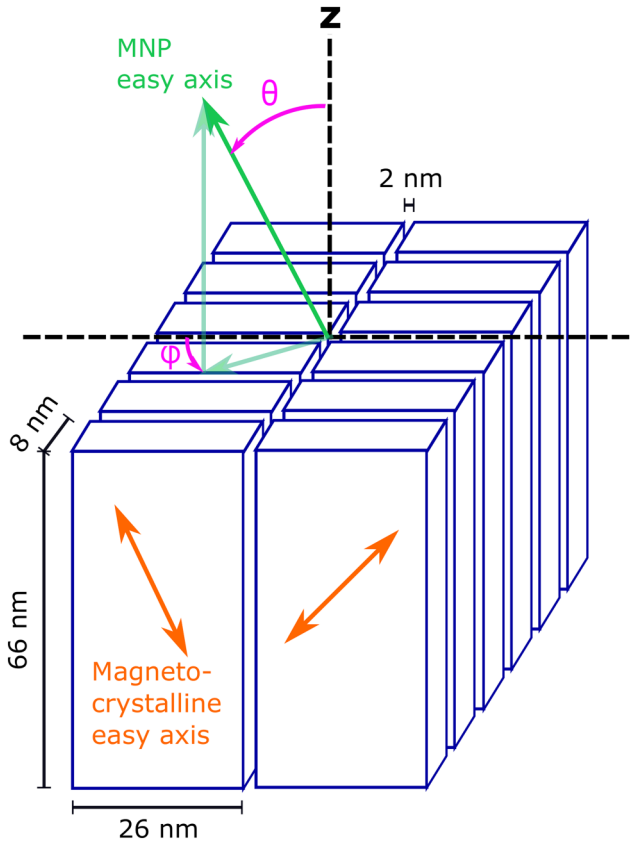

FIG. 1. Schematic of the magnetic model of a BNF MNP, composed of parallelepiped-shaped crystallites of magnetite separated by nonmagnetic regions. The dimensions of the parallelepipeds are from experimentally determined parameters.[28] Each parallelepiped is given a randomly oriented magnetocrystalline anisotropy easy axis, shown in orange on the diagram. The diagram also shows the overall magnetic easy axis of the model MNP as a whole, in green, somewhat offset from the long axis of the parallelepipeds due to the random magnetocrystalline anisotropy of each parallelepiped. In the model, we use the angles θ, defined as the polar angle from the z axis (the long axis of the parallelepipeds), and ϕ, the azimuthal angle in the x–y plane.

C. Micromagnetic simulations

1. Simulation details

We used micromagnetics (OOMMF[20]) to simulate the magnetization of BNF MNPs, modeling the experimentally observed intraparticle and interparticle magnetic structure. The exact structure of the real system is complex (see Sec. II A and associated Refs. 24 and 26–29), so we constructed a reasonable but simplified, computationally feasible model of the internal magnetic structure.

In short, in the real system, each MNP is formed from parallelepiped-shaped crystallites; the magnetic domains are also parallelepiped-shaped but with somewhat different dimensions. Thus, in the real system, the domain boundaries and crystalline grain boundaries are not necessarily coincident. Our simplified model includes parallelepiped-shaped crystallites of magnetite separated by small regions of nonmagnetic material to represent domain boundaries, a reasonable description based on the experimental work.[28] The magnetite crystallites within the model are 66 nm × 26 nm × 8 nm. Each MNP is composed of 12 such parallelepipeds separated by a 2 nm nonmagnetic region such that each MNP is 66 nm × 54 nm × 58 nm (Fig. 1). A few additional simulations were performed using crystallites with dimensions $\pm 1\sigma$ from these average dimensions (e.g., 76 nm × 24 nm × 7 nm and 56 nm × 28 nm × 9 nm) in order to estimate uncertainties due to polydispersity in the simulation results.

The saturation magnetization was that of bulk magnetite at low temperature,[39–42] $M_s = 5 \times 10^5$ A/m. (The bulk value for saturation magnetization was used for the simulation rather than the experimentally measured value for consistency, and also due to the uncertainty in the experimental value for saturation magnetization in this MNP system due to the difficulty of properly normalizing the experimental data to magnetite content while substracting off diamagnetic background contributions for the water and dextran.) Six-neighbor (nearest-neighbor) exchange was used, with an exchange stiffness[43] of $A = 1.2 \times 10^{-11}$ J/m in the magnetic regions and $A = 0$ in the nonmagnetic regions. A 2 nm discretization size was used. Uniaxial magnetocrystalline anixotropy was used, with a value[43] of

$K_u = 6 \times 10^4$ J/m^3, an estimated value for low-temperature magnetite which is expected to differ from the room-temperature value. (The magnetocrystalline anisotropy for magnetite is difficult to determine, and there has been extensive disagreement in the literature showing anomalously large and small values.[30] The value used here is an approximation.)

Within each parallelepiped in the model, the magnetocrystalline anisotropy was defined to be uniform and oriented along a direction randomly chosen on the unit sphere so that the spin structure within each parallelepiped is often approximately collinear except near edges (e.g., Fig. 9). Thus, in the micromagnetic model, each parallelepiped tends to have collinear magnetization within it, similar to a domain, though the region of collinear magnetization is defined by the nonmagnetic boundary rather than spontaneously occurring due to energetics like domains in a perfect bulk crystal. That is, in the model the crystalline grain boundaries and "domain" boundaries are generally coincident, a simplification from the real system.

Because of the random choice of magnetocrystalline anisotropy direction for each of the 12 parallelepipeds comprising the MNP, there are an infinite number of unique MNPs which may be modeled. Thus, each simulation was repeated multiple times with different random number generator seed values and the results averaged in order to make more general conclusions.

2. Calculation of magnetic anisotropy energy

To find the magnetic anisotropy energy, we calculated the energy in OOMMF under an applied field of 10 T (at which the magnetization is well saturated within the simulation), as a function of magnetization direction using 3.75° angular increments, for a total of 4560 field directions in one hemisphere. The other hemisphere is then found by symmetry. The simulation includes four types of energy: Zeeman energy (due to the applied field), demagnetization energy (related to shape anisotropy), magnetocrystalline anisotropy energy, and exchange energy. At 10 T, the spins are closely aligned with the applied field for all field directions. Thus, the magnitude of both the Zeeman energy and the exchange energy varies negligibly with any change in the direction of the applied magnetic field, because the angle between the spins and the field is zero. The variation in Zeeman and exchange energies is 2 and 4 orders of magnitude lower, respectively, than the variation in demagnetization energy and magnetocrystalline anisotropy energy, which are of roughly similar magnitude. Thus, we define the total anisotropy energy as the sum of the demagnetization energy and magnetocrystalline anisotropy; this can be thought of as an effective anisotropy incorporating both shape and magnetocrystalline factors. The total anisotropy energy as a function of field direction was calculated for 109 unique MNPs. The lowest energy directions ("easy axes") and highest energy directions ("hard axes") were tabulated.

3. Calculation of M(H): Particle orientation

In order to study the effect of MNP easy-axis orientation (texture) on the magnetic hysteresis loop of BNF MNPs, we looked more closely at 20 unique MNPs. For each MNP, we found the simulated easy axis as described above and then defined a new primed coordinate system (θ', ϕ'), in which the z' axis ($\theta' = 0$) is parallel to the simulated easy axis. As shown in Fig. 7(a), θ' is the polar angle (from z') and ϕ' is the azimuthal angle (in the x'–y' plane) as usual. Then, we simulated a DC $M(H)$ loop by equilibrating the magnetization at each field step from 1 T to −1 T to 1 T in 20 mT steps. Like the previous simulations, the $M(H)$ simulations also included Zeeman, demagnetization, magnetocrystalline anisotropy, and exchange energy terms. $M(H)$ was simulated for field directions spanning $\theta' = 0°$– 90° and $\phi' = -180°$–180°, in 15° increments. $M(H)$ was calculated along these directions for each unique MNP individually and then summed for the 20 MNPs to find an average $M(H)$ of those 20 MNPs to account for the variability in $M(H)$ between unique MNPs. Interactions between MNPs are considered in Sec. II C 4.

To simulate partial orientation of easy axes (texture), we summed the $M(H)$ loops for field directions within a given polar angle θ'_{max}, weighted by the solid angle as shown in Fig. 7(a). The contribution from hysteresis loops at the boundary of a given θ'_{max} region is given half the usual solid angle because only half of the solid angle is contained within θ'_{max}.

4. Calculation of M(H): Chaining

We modeled $M(H)$ of chains of MNPs using the same method. To simulate chaining, we modeled a linear chain of

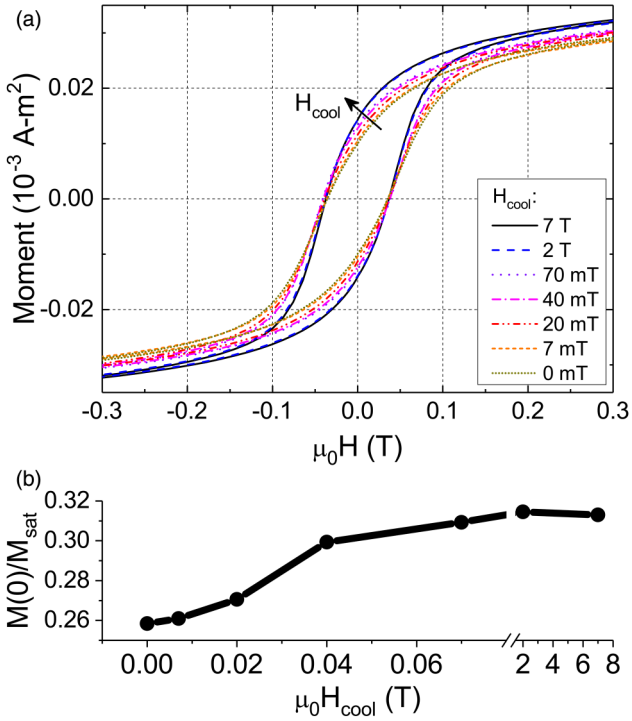

FIG. 2. (a) Experimental hysteresis loops of sample at 11 K for different single-step cooling fields H_{cool}. The hysteresis loops shown are the fifth cycle for each cooling field. The arrow indicates increasing H_{cool}. (b) Remanence $M(0)/M_{sat}$ of hysteresis loops as a function of cooling field. Error bars represent 1σ and are shown; however, they may be smaller than the symbol.

5 MNPs, each with the same parallelepiped-based geometry as used in Sec. II C 3 and varied the spacing to change the strength of the interparticle interaction. The long axes of the parallelepipeds and the chain axis were both parallel to the direction of the field, as shown in Fig. 8(a). For this simulation, each MNP within each simulation is unique so that each chain is unique. We calculated $M(H)$ for 12 unique chains of 5 particles each and averaged them.

III. RESULTS

A. Experimental results

The experimental $M(H)$ loops for the nanoparticle samples are shown in Fig. 2(a). A trend is observed in which the hysteresis loops measured after cooling in a large field are more square shaped, while the hysteresis loops measured after cooling in a small or zero field are more stretched along the diagonal. To illustrate this, the remanence $M(0)/M_{sat}$ is shown as a function of cooling field in Fig. 2(b). The remanence clearly increases with increased cooling field, due to the increased squareness of the hysteresis loops measured at high fields. This indicates a change in the magnetic anisotropy along the field direction when the sample is frozen in an applied field compared to when it is frozen in zero field. We speculate that this could be explained by orientation of the individual MNP's easy axis along the direction of the field or by the chains formed in the direction of the field, or both.

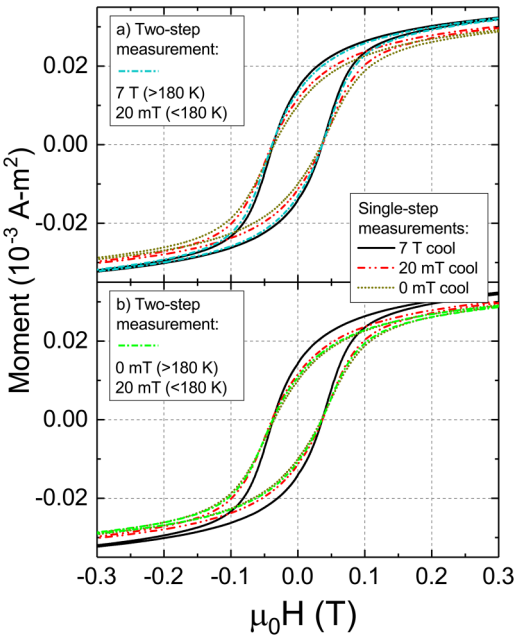

FIG. 3. Experimental hysteresis loops at 11 K for the cases where the sample was cooled by a two-step process: (a) Cooled from 300 K to 180 K in 7 T and from 180 K to 11 K in 20 mT. (b) Cooled from 300 K to 180 K in 0 mT and from 180 K to 11 K in 20 mT. These data are compared to selected data from the single-step cooling from Fig. 2. All the hysteresis loop data shown here are from the fifth field cycle for each cooling condition.

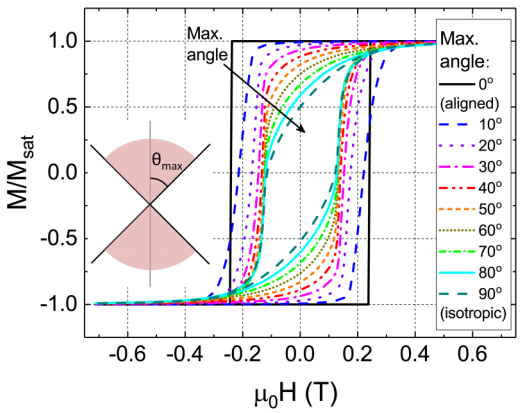

FIG. 4. Calculated $M(H)$ for ensembles of identical, noninteracting Stoner-Wohlfarth MNPs having easy axes randomly distributed within a given maximum angle from the field axis. Here, the H axis is scaled assuming material parameters of magnetite. The arrow indicates increasing maximum angle.

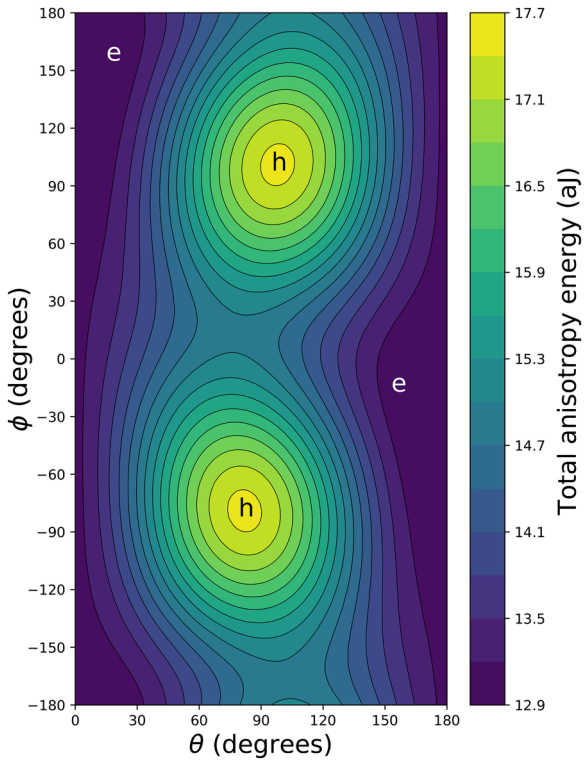

FIG. 5. Total anisotropy energy (demagnetization plus magnetocrystalline anisotropy energy) of one MNP as a function of applied field direction. The white e's indicate the minimum energy (easy axes), while the black h's indicate the maximum energy (hard axes). Zeeman energy is not included; it is large, negative, and does not vary significantly as a function of angle. Exchange energy is also not included; it is small and does not vary significantly as a function of angle.

The data from the two-step field cooling procedure yield an additional insight. These data are shown in Fig. 3. It was found that the hysteresis loops from the two-step cooling experiments most closely resemble the hysteresis loops from the one-step cooling experiments which have the same field during the "physical freezing" of the sample (i.e., during cooling from 300 K to 180 K), regardless of the field below the phase transition, as shown in Fig. 3. This supports the idea that the shape change of the hysteresis loop upon field cooling is primarily due to physical rearrangement of MNPs in a field, i.e., chaining or orientation of overall magnetic anisotropy axes, which is frozen in place at the physical freezing point of H_2O. In contrast, if the opposite result had been found, it would imply that "magnetic freezing" was the most important contributor to the shape of the hysteresis loop, which may occur in systems with a spin or superspin glass component.[34,35]

B. Simulation results

As described in Sec. III A, we use simulations to consider two effects to explain the changes in hysteresis loop shape with different field cooling: orientation of MNPs' easy axes and MNP chaining. In the process of studying the effect of MNP orientation, we also analyzed the magnetic anisotropy behavior of the individual MNPs.

1. Magnetic easy-axis orientation

When a magnetic field is applied to MNPs which are free to rotate physically (as is the case for the BNFs in H_2O at 300 K), we expect that the individual MNP's easy axis may align along the direction of the field (texturing).[44] When the suspension is then cooled, this field-induced magnetic texture can be locked-in. For a single-domain MNP with uniaxial anisotropy, texturing may be described by the Stoner-Wohlfarth model, with the well-known result of a square hysteresis loop for completely oriented MNPs and diagonal loops for completely misoriented MNPs. The $M(H)$ loops for different orientations can be summed, weighted by the solid angle, to find $M(H)$ loops for ensembles of MNPs. Figure 4 shows $M(H)$ for ensembles of noninteracting Stoner-Wohlfarth MNPs with easy axes randomly oriented within a given maximum angle from the field direction. A uniform distribution of easy axes within the maximum angle was used for the calculation. A maximum angle of 90° yields the familiar curve for the isotropic (completely randomly oriented) case.[10] The Stoner-Wohlfarth model does not describe well the experimental $M(H)$ loops of the BNF MNPs. The Stoner-Wohlfarth $M(H)$ loops are very upright with a steep slope of $M(H)$ near $M = 0$, and they saturate at relatively low fields. On the other hand, the experimental $M(H)$ loops are more skewed/diagonal with a

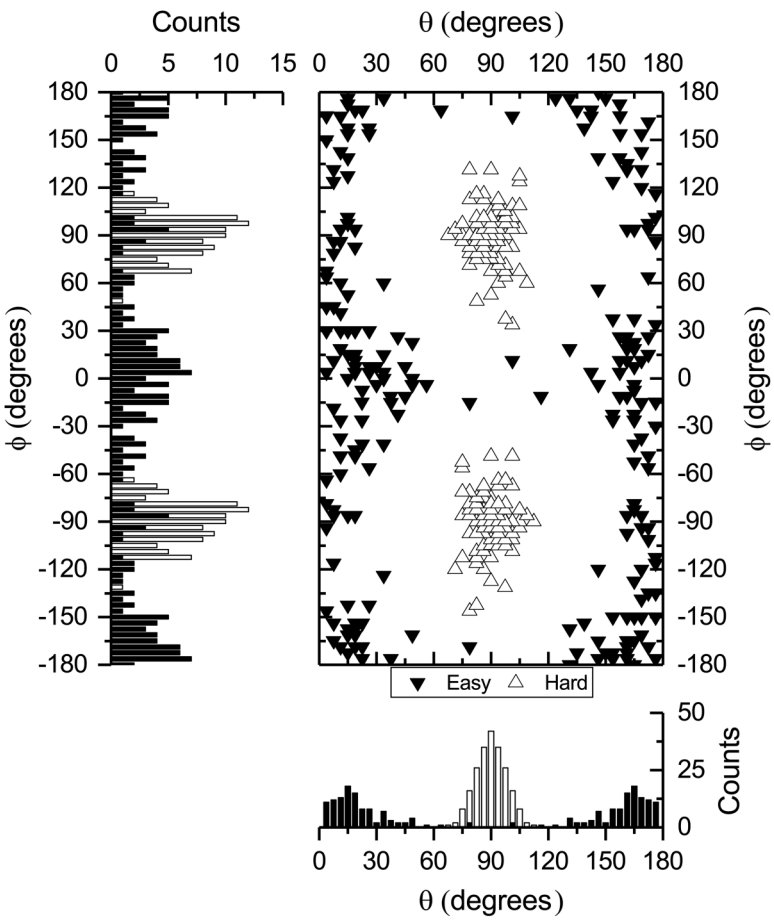

FIG. 6. The easy (black) and hard (white) directions (θ, ϕ) of 109 unique MNPs. Frequency of occurrence of easy (black) and hard (white) directions in θ and ϕ are shown on the bottom and left side, respectively. θ and ϕ are defined in Fig. 1.

shallow slope of $M(H)$ near $M = 0$. In addition, the experimental $M(H)$ loops have a long tail as they approach saturation.

As a result, we have studied here the effects of orientation and texturing using the micromagnetic model. First, we determine the effective anisotropy energy of the particle as a whole, as described in Sec. II C 2. For our model MNPs, based on the geometry shown in Fig. 1, we expect that shape anisotropy due to demagnetization energy is triaxial, with the lowest overall energy orientation (the "easy" axis) when the magnetization is parallel to the long axis of the parallelepipeds ($\theta = 0°$ or $180°$). Likewise, the highest overall energy orientation (the "hard" axis) would be when the magnetization is parallel to the short axis ($\theta = 90°$ and $\phi = \pm 90°$). However, this energy landscape is modified by the magnetocrystalline anisotropy energy of each parallelepiped, which is unique to each MNP based on the random orientation of the magnetocrystalline anisotropy axes. This is shown, for a typical MNP, in Fig. 5. The resulting energy landscape looks similar to that expected based on shape anisotropy, but energy maxima and minima are shifted. Specifically, for one typical MNP shown here (Fig. 5), the easy axis occurs at $\theta = 15°$ rather than $\theta = 0°$ as would be expected based solely on shape anisotropy.

The easy and hard directions are given by (θ, ϕ) as defined in Fig. 1. The distribution of θ and ϕ values for the 109 simulated MNPs is shown in Fig. 6, showing that the easy directions are clustered around $\theta = 0°$ and $\theta = 180°$. In the upper hemisphere, θ values for easy directions range between 3.75° and 75.00°, with a statistical mean of 20° and a statistical median and mode of 15°. The easy directions span the entire range of ϕ, but somewhat more frequently occur around $\phi = 0$ and $\pm 180°$. The hard directions are strongly clustered around $\theta = 90°$ and $\phi = \pm 90°$. This is not surprising due to the energy penalty of the short axis of the parallelepiped at $\theta = 90°$, $\phi = \pm 90°$. Competition between shape and magnetocrystalline anisotropy has been discussed by other researchers. Because of the wide variation in magnetic structure and behavior of MNP systems, the dominant anisotropy will depend on the details of a given system. However, it has been shown that magnetic anisotropy is often more complicated than had been previously considered[30] and magnetocrystalline anisotropy is often dominated by other terms such as shape or colloidal anisotropy.[30,45,46] This is similar to our results.

$M(H)$ when the easy axis of the MNP is oriented along the field direction ($\theta'_{max} = 0$, the fully oriented case) is shown in Fig. 7(b), in black. This simulated $M(H)$ curve displays many more similarities to the experimental data than the Stoner-Wohlfarth model does. In particular, the micromagnetic simulation captures the diagonal shape of the $M(H)$ loop and the shallow slope of $M(H)$ near $M = 0$. The $M(H)$ curves for partial easy-axis orientation are shown in color, with $\theta'_{max} = 90°$ corresponding to the isotropic (completely unoriented) case. The differences between the orientations are much smaller than is seen in the Stoner-Wohlfarth case. However, $M(H)$ for the oriented MNPs has a slightly larger coercivity while the hysteresis loop for the isotropically distributed MNPs has a slightly smaller coercivity, as well as a slight change in the approach to saturation, with some similarities to the experimental data shown in Fig. 2. Data in the literature for aligned and unaligned noninteracting MNPs show a similar trend in $M(H)$ in which coercivity decreases as MNP alignment decreases.[47,48]

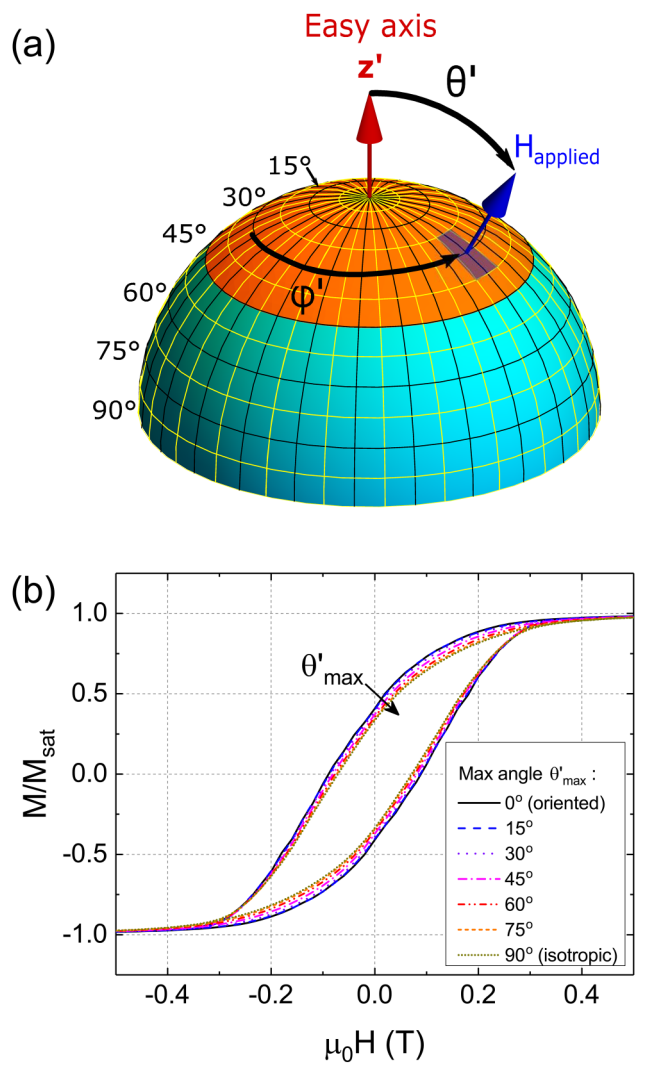

FIG. 7. (a) Schematic of angles used for hysteresis loop simulations. θ' is the polar angle, defined as the angle from the easy axis of the MNP (z' axis). ϕ' is the azimuthal angle in the $x' - y'$ plane. The black lines delineate 15° increments; $M(H)$ was simulated along directions at the intersections of the black lines. This schematic shows, in orange, the field directions that are included in the sum to obtain the hysteresis loop for an ensemble with a maximum angle $\theta'_{max} = 45°$. The hysteresis loops included in the sum are weighted by the solid angle. The schematic shows, highlighted in purple, the solid angle that is attributed to a single field direction at $\theta' = 30°$, indicated by a blue arrow. (b) Simulated $M(H)$, the average of $M(H)$ calculated for 20 unique MNPs for a range of values of θ'_{max}. The arrow indicates increasing θ'_{max}.

2. Chaining

It has been shown experimentally that, under an applied magnetic field, the BNF MNPs rearrange into long chains, loosely oriented along the field direction.[29,30] These chains, via their increased dipolar interactions, add an additional effective term(s) in the

anisotropy energy, which can be called colloidal anisotropy.[49–51] In this section, we model chains of MNPs and show that chaining reduces the skew effect in the $M(H)$ loops. As described in Sec. II C 4 and shown in Fig. 8(a), we modeled chains of 5 parallelepiped-based MNPs in which the long axes of the parallelepipeds and the chain axis were both parallel to the direction of the field. From the result of Sec. III B 1, we know that the easy axis of the simulated MNP typically points around ≈15° from the long axis of the parallelepipeds, so the simplifying approximation to align the parallelepiped long axis along the field direction is reasonable. The resulting $M(H)$ is shown in Fig. 8(b) for a range of interparticle spacings. Each MNP is 66 nm in length so that the closest MNPs, with 68 nm spacing (center-to-center), are nearly touching. The $M(H)$ loops become more diagonal and less square with an increase in spacing, again showing some similarities to the experimental data in Fig. 2.

To understand the differences in $M(H)$, we can look at the individual spins in the micromagnetic simulation. A map of the spins in a slice [Fig. 8(a)] through the middle simulated MNP (out of the chain of 5 MNPs) is shown in Fig. 9 for the $H = 0$ mT step of a hysteresis loop simulation, after having applied an initial saturating field of 1 T in the positive direction (up). The intraparticle structure of magnetic parallelepipeds with nonmagnetic spacers leads to an interruption of the exchange interaction between parallelepipeds. Thus, parallelepipeds only interact with each other via dipolar interactions. The simulated spins tend to orient within the plane of the parallelepipeds (up/down and in/out of the page), with only small components of the magnetization vector pointing along the short direction of the parallelepiped (left/right). This is in agreement with previous experimental results.[28]

Dipolar interactions between side-by-side parallelepipeds should favor antiparallel alignment because it reduces demagnetization energy; however, the randomly oriented magnetocrystalline anisotropy axes and the magnetic field history prevent a fully antiparallel alignment. In Fig. 9(a), which shows an isolated MNP (300 nm spacing), only two of the six parallelepipeds have largely reversed their magnetization from the direction of the originally applied field.

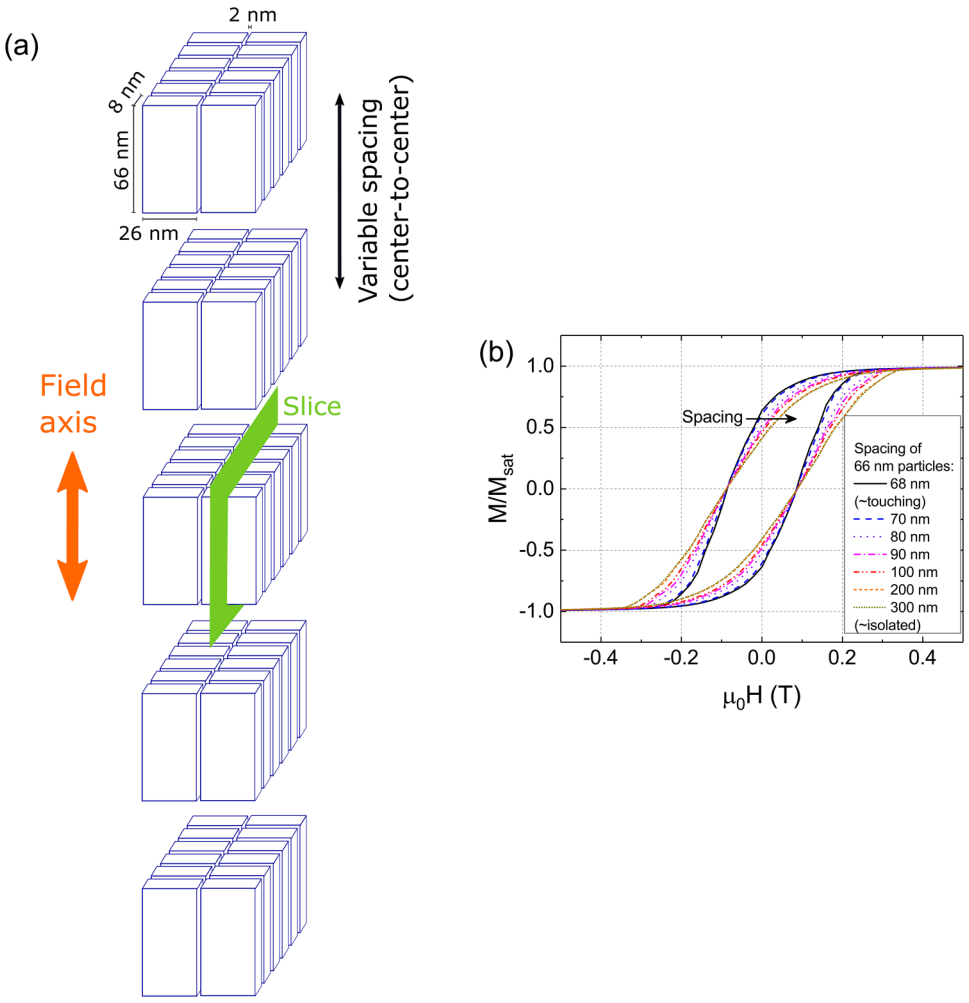

FIG. 8. (a) Geometry for simulations of chains of 5 MNPs. The field, linear chain direction, and long axes of parallelepipeds are all parallel. The slice of spins shown in Fig. 9 is indicated in green in this diagram. (b) Average of simulated hysteresis loops for 12 unique chains of 5 interacting MNPs each, for a range of MNP spacing. MNP spacing is given as the center-to-center distance between 66 nm MNPs. The arrow indicates increasing spacing.

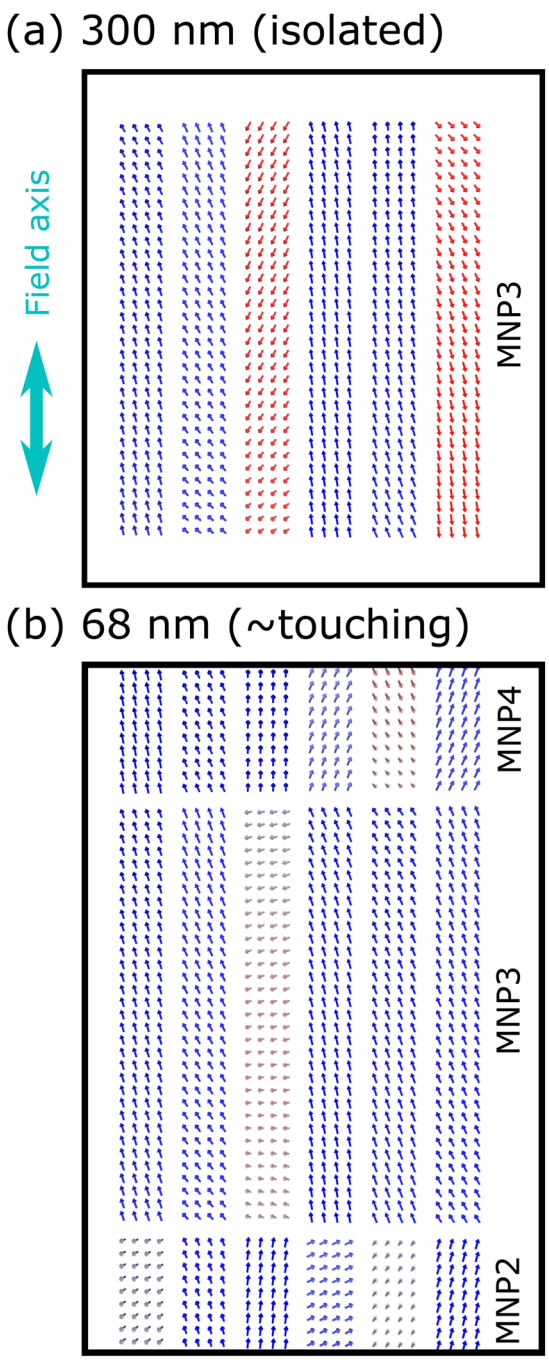

FIG. 9. Slice through the 3rd (middle) parallelepiped-based MNP in a chain of 5 from the OOMMF simulation for $H = 0$ mT, shown in Fig. 8. A field of 1 T was initially applied in the $+z$ direction (up) and was decreased to $H = 0$ mT, shown here. In this color scheme, blue indicates spins pointing up, and red indicates spins pointing down. Gray indicates spins pointing in or out of the page. This is shown for two interparticle spacings: (a) 300 nm (isolated) and (b) 68 nm (strongly interacting). In (b), the edges of the neighboring MNPs are also visible in the figure.

Figure 9(b) shows the same simulated MNP with close spacing (68 nm), i.e., strong interparticle interactions. The edges of the neighboring MNPs in the chain can be seen at the top and bottom of the frame. In this case, the head-to-tail interactions between neighboring MNPs tend to favor parallel alignment, and none of the parallelepipeds have completely reversed their magnetization direction, though some have significant components of the magnetization pointing in/out of the page.

These dipolar interactions are responsible for a lower remanence (at $H = 0$ mT) than would be expected for a single-spin, coherent rotation model. They are also responsible for a more gradual magnetization reversal than is seen in a Stoner-Wohlfarth model. This effect is similar to that seen for certain spatial arrangements of monolithic MNPs in other studies.[15,52,53]

IV. DISCUSSION

To compare $M(H)$ from our experimental data with $M(H)$ from the theoretical models, we use the remanence $M(0)/M_{sat}$, the reduced susceptibility $d(M/M_{sat})/d(\mu_0 H)$ at $M = 0$, and the coercivity H_c as metrics.

The remanence is shown in Fig. 10. In the experimental data, $M(0)/M_{sat}$ increases as the cooling field increases. In the easy-axis orientation model, $M(0)/M_{sat}$ increases slightly as the MNPs become more oriented and in the chaining model, $M(0)/M_{sat}$ increases as the spacing becomes smaller. Both increased alignment and increased chaining would be expected to occur in a larger cooling field, so both models are consistent with the experimental data. These data show that chaining can have a larger, more significant effect than orientation on the remanence.

The reduced susceptibility is shown in Fig. 11. Experimentally, the slope of the hysteresis loop $d(M/M_{sat})/d(\mu_0 H)$ at $M = 0$ increases with cooling field, leveling off at the highest field. $d(M/M_{sat})/d(\mu_0 H)$ barely changes as orientation changes; however, it increases significantly with chaining. Thus, the trend in reduced susceptibility can be explained primarily by chaining, with the presence of dextran preventing the smallest spacings from being realized and stabilizing the system.

The coercivity is shown in Fig. 12. In the experimental data, H_c is essentially unchanged (within the uncertainty) as a function of cooling field. In the easy-axis orientation model, H_c increases with orientation while in the chaining model, H_c remains nearly constant as MNP spacing becomes smaller. The latter could be correlated with a higher cooling field. Therefore, chaining is likely to be the dominant factor controlling the behavior of H_c seen in the experimental data. However, coercivity is notoriously difficult to model.[11,54]

The energies involved in both the overall easy-axis orientation of individual MNPs in a field and the dipole-dipole interaction between MNPs are both significantly larger than the thermal energy in this system. At freezing ($\approx$270 K), thermal energy is $k_B T = 3.7 \times 10^{-21}$ J. The anisotropy energy difference $\Delta E_{anis} \approx 5 \times 10^{-18}$ J for a typical model MNP (see Fig. 5). The Zeeman energy and the dipole-dipole interaction energy both rely on the total magnetic moment m for the MNP, which may be calculated to be $m \approx 8 \times 10^{-17}$ A m^2 at saturation from the magnetization and volume of the model MNP given in

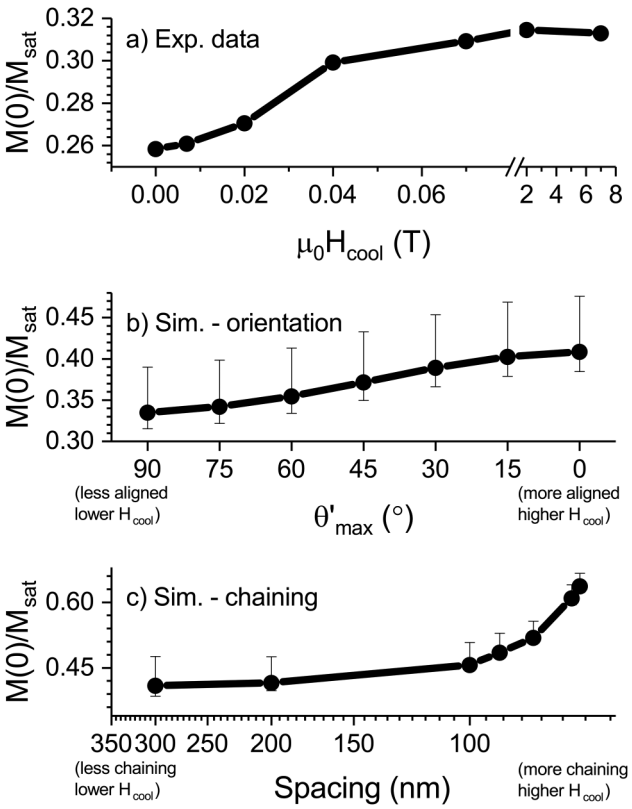

FIG. 10. Remanence of hysteresis loops for (a) experimental data, as a function of cooling field, (b) micromagnetic simulations of noninteracting MNPs as a function of angle, and (c) micromagnetic simulations for chains of 5 MNPs, as a function of interparticle spacing. Error bars represent 1σ and are shown; however, they may be smaller than the symbol. For (b) and (c), error bars represent uncertainty due to polydispersity (see Sec. II C 1).

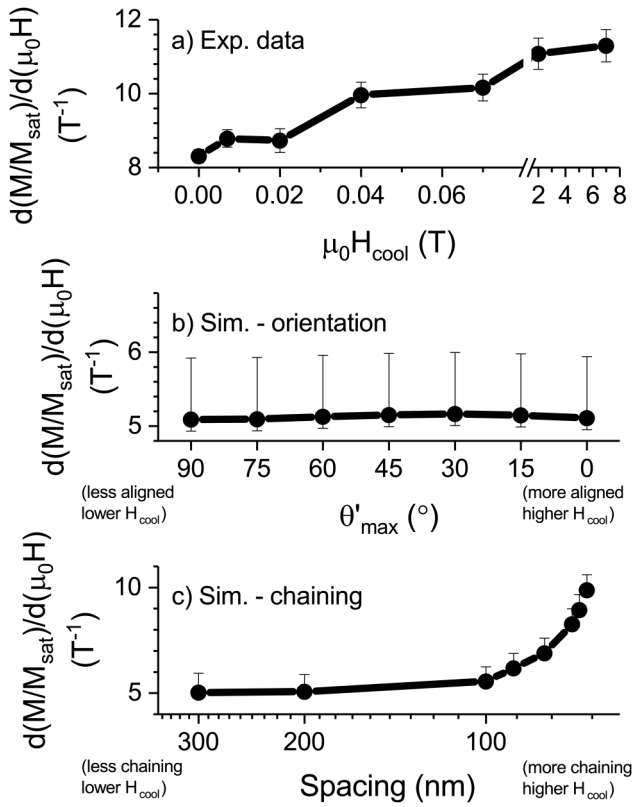

FIG. 11. Reduced susceptibility $d(M/M_{sat})/d(\mu_0 H)$ at $M = 0$ of hysteresis loops for (a) experimental data, as a function of cooling field, (b) micromagnetic simulations of noninteracting MNPs as a function of angle, and (c) micromagnetic simulations for chains of 5 MNPs, as a function of interparticle spacing. Error bars represent 1σ and are shown; however, they may be smaller than the symbol. For (b) and (c), error bars represent uncertainty due to polydispersity (see Sec. II C 1).

Sec. II C 1. The Zeeman energy in an external field is then $E_Z \approx 6 \times 10^{-19}$ to 6×10^{-16} J for fields between 7 mT and 7 T. The dipole-dipole interaction energy is $E_{dip} \approx 3\mu_0 m^2/4\pi r^3$, which is approximately 7×10^{-20} J to 7×10^{-18} J for center-to-center interparticle spacings from 300 to 66 nm, as considered by our chaining model. Note that all the energies discussed here are larger than $k_B T$ so that it is reasonable to expect the MNPs magnetic moments to align along the overall MNP easy axis (at saturating fields) and for those easy axes to align along the direction of the field. Dipole-dipole interactions resulting in MNP chaining are also reasonably expected for the interparticle spacings considered here, though the smallest spacings considered theoretically are likely disallowed experimentally by the thick dextran coating. In order for the dipole-dipole interaction energy to decrease to the level of the thermal energy, the interparticle spacing would need to increase to 800 nm (larger than any considered here and corresponding to a dilute MNP concentration of about 1 mg/ml). In such a dilute case, chaining would be unlikely to occur. An important caveat to these order-of-magnitude calculations is that, should an individual MNP be demagnetized, with the internal regions of nonuniform magnetization cancelling each other, the anisotropy energy as we have considered it is not well-defined. In addition, Zeeman and dipole-dipole interaction energies, which depend on a total moment m for the MNP, could be much smaller. However, the remanence of both individual and chained model MNPs, as well as the experimental system, is significant ($\approx \frac{1}{3} M_{sat}$) such that MNPs will likely be sensitive to easy-axis orientation and dipole-dipole interaction, once magnetized, even in very small fields.

Our results highlight the importance of the geometry of intraparticle and interparticle structures on the shape of the hysteresis loop. Qualitatively, the trends observed here should apply generally to internally structured, interacting MNPs in the same size range (~50 nm) with competing anisotropies (shape and magnetocrystalline). In particular, intraparticle structure leads to a diagonal-shaped hysteresis loop distinctly different from that

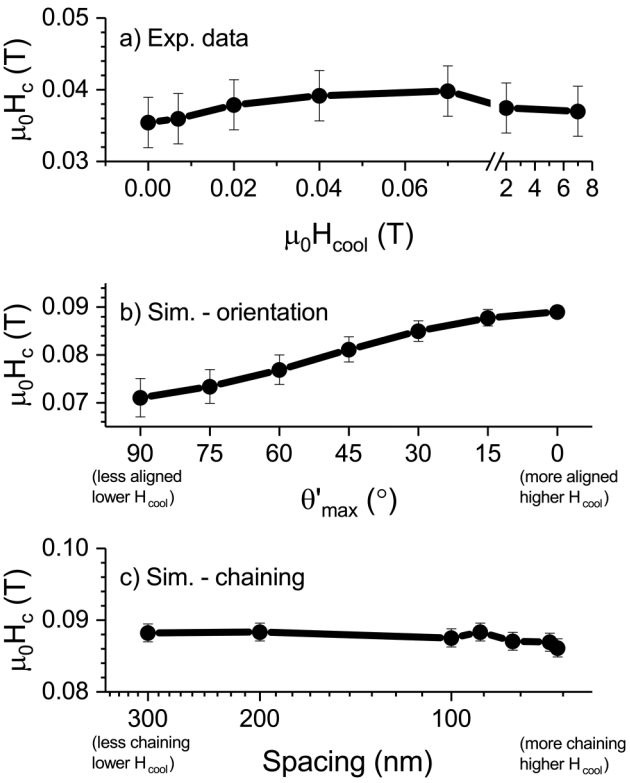

FIG. 12. Coercivity of hysteresis loops for (a) experimental data, as a function of cooling field, (b) micromagnetic simulations of noninteracting MNPs as a function of angle, and (c) micromagnetic simulations for chains of 5 MNPs, as a function of interparticle spacing. Error bars represent 1σ and are shown. For (b) and (c), error bars represent uncertainty due to polydispersity (see Sec. II C 1).

obtained by the Stoner-Wohlfarth model, interparticle interactions in the form of chains decrease the skew of the hysteresis loop, and easy-axis orientation increases the coercivity. These qualitative trends are generally expected to translate to application conditions, in particular, the conditions of hyperthermia treatment, based on the discussion in Sec. I. Differences may occur, however, depending on the specifics of the MNP environment. Importantly, the degree of mobility of MNPs in a fluid vs a tissue environment will determine whether the MNPs form chains or other structures. Our results show the importance of the geometry of such structures to the resulting $M(H)$.

Although the qualitative trends in remanence, reduced susceptibility, and coercivity are suggestive of a combination of MNP easy-axis orientation and chaining leading to the observed experimental behavior, the quantitative values for these metrics differ between theory and experiment. This suggests that further effects influence $M(H)$ in the complex experimental system which are not taken into account by this micromagnetic model of MNPs with parallelepiped-shaped magnetic structures. These likely include MNP nonuniformity, interchain interactions, surface effects, and finite-temperature effects.

V. CONCLUSION

In summary, the MNP system studied here, composed of BNF MNPs, does not behave as Stoner-Wohlfarth model particles. The shape of the hysteresis loop can be modeled micromagnetically, taking into account the internal magnetic structure of the MNPs. Parallelepiped-shaped magnetic structures prevent magnetization reversal by coherent rotation. Our model found that variation in the orientation of the overall MNP magnetic easy axes (texture) primarily changes the coercivity of the MNPs hysteresis loops, while MNP chaining primarily impacts the approach to saturation. The trends in experimentally measured hysteresis loops are most likely explained by a combination of texturing and chaining, with chaining playing a dominant role. This has implications for all applications of MNPs, including hyperthermia, imaging, and data storage.

ACKNOWLEDGMENTS

Zoe Boekelheide and Jackson T. Miller acknowledge the Computational Physics Laboratory at Lafayette College for the computing power used for the modeling portion of the work and thank Andrew Dougherty for supporting the Linux cluster.

REFERENCES

[1] R. K. Gilchrist, R. Medal, W. D. Shorey, R. C. Hanselman, J. C. Parrott, and C. B. Taylor, Ann. Surg. **146**, 596 (1957).
[2] E. A. Perigo, G. Hemery, O. Sandre, D. Ortega, E. Garaio, F. Plazaola, and F. J. Teran, Appl. Phys. Rev. **2**, 041302 (2015).
[3] J.-E. Kim, J.-Y. Shin, and M.-H. Cho, Arch. Toxicol. **86**, 685 (2012).
[4] P. C. Lauterbur, Nature **242**, 190 (1973).
[5] B. Gleich and J. Weizenecker, Nature **435**, 1214 (2005).
[6] K. Raj and R. Moskowitz, IEEE Trans. Magn. **MAG-16**, 358 (1980).
[7] Y. T. Choi and N. M. Werely, J. Aircr. **40**, 432 (2003).
[8] N. A. Usov, M. L. Fdez-Gubieda, and J. M. Barandiaran, J. Appl. Phys. **113**, 023907 (2013).
[9] J. W. F. Brown, Ann. N.Y. Acad. Sci. **147**, 461 (1969).
[10] E. C. Stoner and E. P. Wohlfarth, Philos. Trans. R. Soc. Lond. Ser. A **240**, 599 (1948).
[11] R. Skomski, *Simple Models of Magnetism* (Oxford University Press, 2008).
[12] J. Carrey, B. Mehdaoui, and M. Respaud, J. Appl. Phys. **109**, 083921 (2011).
[13] S. Ruta, R. Chantrell, and O. Hovorka, Sci. Rep. **5**, 9090 (2015).
[14] C. Martinez-Boubeta, K. Simeonidis, A. Makridis, M. Angelakeris, O. Iglesias, P. Guardia, A. Cabot, L. Yedra, S. Estrade, F. Peiro *et al.*, Sci. Rep. **3**, 1652 (2013).
[15] D. Serantes, K. Simeonidis, M. Angelakeris, O. Chubykalo-Fesenko, M. Marciello, M. del Puerto Morales, D. Baldomir, and C. Martinez-Boubeta, J. Phys. Chem. C **118**, 5927 (2014).
[16] Z. Nedelkoski, D. Kepaptsoglou, L. Lari, T. Wen, R. A. Booth, S. D. Oberdick, P. L. Galindo, Q. M. Ramasse, R. F. L. Evans, S. Majetich *et al.*, Sci. Rep. **7**, 45997 (2017).
[17] T. L. Gilbert and J. M. Kelly, *Anomalous Rotational Damping in Ferromagnetic Sheets* (American Institute of Electrical Engineers, 1955).
[18] T. L. Gilbert, IEEE Trans. Magn. **40**, 3443 (2004).
[19] A. Vansteenkiste, J. Leliaert, M. Dvornik, M. Helsen, F. Garcia-Sanchez, and B. V. Waeyenberge, AIP Adv. **4**, 107133 (2014).
[20] M. J. Donahue and D. G. Porter, Tech. Rep. Interagency Report NISTIR 6376, National Institute of Standards and Technology, Gaithersburg, MD, 1999.
[21] R. F. L. Evans, W. J. Fan, P. Chureemart, T. A. Ostler, M. O. A. Ellis, and R. W. Chantrell, J. Phys. Condens. Matter **26**, 103202 (2014).
[22] R. Yanes, O. Chubykalo-Fesenko, H. Kachkachi, D. A. Garanin, R. Evans, and R. W. Chantrell, Phys. Rev. B **76**, 064416 (2007).

[23]A. Attaluri, S. K. Kandala, M. Wabler, H. Zhou, C. Cornejo, M. Armour, M. Hedayati, Y. Zhang, T. L. DeWeese, C. Herman *et al.*, Int. J. Hyperthermia **31**, 359 (2015).
[24]C. L. Dennis, A. J. Jackson, J. A. Borchers, P. J. Hoopes, R. Strawbridge, A. R. Foreman, J. van Lierop, C. Grüttner, and R. Ivkov, Nanotechnology **20**, 395103 (2009).
[25]C. Haase and U. Nowak, Phys. Rev. B **85**, 045435 (2012).
[26]C. Grüttner, K. Müller, J. Teller, F. Westphal, A. Foreman, and R. Ivkov, J. Magn. Magn. Mater. **311**, 181 (2007).
[27]K. L. Krycka, A. J. Jackson, J. A. Borchers, J. Shih, R. Briber, R. Ivkov, C. Grüttner, and C. L. Dennis, J. Appl. Phys. **109**, 07B513 (2011).
[28]C. L. Dennis, K. L. Krycka, J. A. Borchers, R. D. Desautels, J. van Lierop, N. F. Huls, A. J. Jackson, C. Grüttner, and R. Ivkov, Adv. Funct. Mater. **25**, 4300 (2015).
[29]Z. Boekelheide and C. L. Dennis, AIP Adv. **6**, 085201 (2016).
[30]C. L. Dennis, A. J. Jackson, J. A. Borchers, C. Grüttner, and R. Ivkov, Nanotechnology **29**, 215705 (2018).
[31]C. L. Dennis, A. J. Jackson, J. A. Borchers, R. Ivkov, A. R. Foreman, P. J. Hoopes, R. Strawbridge, Z. Pierce, E. Goerntiz, J. W. Lau *et al.*, J. Phys. D Appl. Phys. **41**, 134020 (2008).
[32]D. E. Bordelon, C. Cornejo, C. Grüttner, F. Westphal, T. L. DeWeese, and R. Ivkov, J. Appl. Phys. **109**, 124904 (2011).
[33]Certain commercial equipment, instruments, or materials are identified in this paper to more completely define the experimental setup. Such identification does not imply recommendation or endorsement by the National Institute of Standards and Technology, nor does it imply that the materials or equipment identified is necessarily the best available for the purpose.
[34]J. Nogues, J. Sort, V. Langlais, V. Skumryev, S. Surinach, J. S. Munoz, and M. D. Baro, Phys. Rep. **422**, 65 (2005).
[35]O. Iglesias, A. Labarta, and X. Batlle, J. Nanosci. Nanotechnol. **8**, 2761 (2008).
[36]*VSM Application Note 1096-301 Performing VSM Measurements in PPMS High-Field (14 T or Higher) Magnets* (Quantum Design, 2004).
[37]*MPMS Application Note 1014-208 Remnant Fields in MPMS Superconducting Magnets* (Quantum Design, 2002).
[38]C. Song, B. Cui, H. Y. Yu, and F. Pan, J. Appl. Phys. **114**, 183906 (2013).
[39]J. Smit and H. P. J. Wijn, *Ferrites* (John Wiley and Sons, 1959).
[40]B. A. Calhoun, Phys. Rev. **94**, 1577 (1954).
[41]C. A. Domenicali, Phys. Rev. **78**, 458 (1950).
[42]P. Kucheryavy, J. He, V. T. John, P. Maharjan, L. Spinu, G. Z. Goloverda, and V. L. Kolesnichenko, Langmuir **29**, 710 (2013).
[43]M. Ziese, R. Hohne, P. Esquinazi, and P. Busch, Phys. Rev. B **66**, 134408 (2002).
[44]A. Urtizberea, A. Arizaga, N. J. O. Silva, A. Millán, F. Palacio, and F. Luis, J. Appl. Phys. **111**, 093910 (2012).
[45]N. A. Usov and J. M. Barandiaran, J. Appl. Phys. **112**, 053915 (2012).
[46]H. Mamiya, J. Nishigaki, M. Fukunaga, I. Furukawa, J. Cuya, and B. Jeyadevan, *Magnetic Properties of Well-Isolated Magnetite Nanoparticles*, paper presented at the International Conference for Fine Particle Magnetism (ICFPM), Gaithersburg, MD, 13 June 2016.
[47]J.-C. Eloi, M. Okuda, S. E. W. Jones, and W. Schwarzacher, Biophys. J. **104**, 2681 (2013).
[48]J.-C. Eloi, M. Okuda, S. C. Carreira, W. Schwarzacher, M. J. Correia, and W. Figueiredo, J. Phys. Condens. Matter **26**, 146006 (2014).
[49]C. L. Dennis and R. Ivkov, Int. J. Hyperthermia **29**, 715 (2013).
[50]Y. Zhang, L. Sun, Y. Fu, Z. C. Huang, X. J. Bai, Y. Zhai, J. Du, and H. R. Zhai, J. Phys. Chem. C **113**, 8152 (2009).
[51]Y. Qi, L. Zhang, and W. Wen, J. Phys. D Appl. Phys. **36**, L10 (2003).
[52]B. Rana, A. Ganguly, and A. Barman, IEEE Trans. Magn. **47**, 2859 (2011).
[53]L.-M. Wang, A. Qdemat, O. Petracic, E. Kentzinger, U. Rücker, F. Zheng, P.-H. Lu, X.-K. Wei, R. E. Dunin-Borkowski, and T. Brückel, Phys. Chem. Chem. Phys. **21**, 6171 (2019).
[54]J. Fischbacher, A. Kovacs, H. Oezelt, M. Gusenbauer, T. Schrefl, L. Exl, D. Givord, N. M. Dempsey, G. Zimanyi, M. Winklhofer *et al.*, Appl. Phys. Lett. **111**, 072404 (2017).